2nd Canadian Conference on
Effective Design of Structures
McMaster University
Hamilton, Ontario, Canada
May 20 – 23, 2008

Understanding the Nano and Micro Structure of Concrete to Improve its Durability

P.J.M. Monteiro[1], A.P. Kirchheim[1], S. Chae[1], P. Fischer[2], A.A. MacDowell[3], E. Schaible[3], H.R. Wenk[4]

[1]Department of Civil and Environmental Engineering, University of California at Berkeley
[2]Center for X-ray Optics, Lawrence Berkeley National Laboratory, Berkeley, CA USA
[3]Advanced Light Source, Lawrence Berkeley National Laboratory, USA
[4]Earth and Planetary Science, University of California at Berkeley

Abstract

New and advanced methodologies have been developed to characterize the nano and microstructure of cement paste and concrete exposed to aggressive environments. High resolution full field soft X-ray imaging in the water window is providing new insight into the cement hydration process on the nano scale. Hard X-ray microtomography results on ice inside cement paste and cracking caused by the alkali-silica reaction (ASR) enables 3dimensional structural identification. The potential of neutron diffraction to determine reactive aggregates by measuring their residual strains and preferred orientation is being explored.

Keywords: concrete, durability, microscopy, neutron, tomography, X-ray

Introduction

Classical studies of the microstructure of cement paste and concrete has been largely done with electron microscopy. The complex nanostructure of calcium silicate hydrates has been investigated by transmission electron microscopy while scanning electron microscopy (both in secondary and backscattered mode) were often used to characterize the phase distributions and to assess damage of the material exposed to aggressive environments. However, the disadvantage of these techniques is that they require a high vacuum which can modify or even damage the fragile hydration products. The existence of high vacuum also prevents the in-situ imaging of the hydration reactions. X-ray based imaging techniques, which are abundantly available at large scale facilities using synchrotron radiation have the potential to revolutionize the current understanding of hydration mechanisms of cements.

We will describe recent work performed at the full-field soft transmission X-ray microscope XM-1 located at beamline 6.1.2 at the Advanced Light Source (ALS) in Berkeley, CA and operated by the Center for X-ray Optics at Lawrence Berkeley National Laboratory since 1994. Originally designed for the observation of biological cells in their natural, wet state at atmospheric pressure it has found wide applications in nanoscience such as nanomagnetism and nanomaterials sciences. It is currently an important facility where numerous studies with cementitious materials have been carried out since 1998 (see e.g. ref. [1-11]). This technique allows high-resolution soft X-ray imaging of cement in aqueous solution and of the early formation of the hydration products.

It is challenging to characterize the 3-dimensional network of microcracks using non-destructive techniques. The traditional method of impregnating the concrete, cutting and polishing the sample can introduce artifacts. Another limitation of this approach is that the observation is only done at the surface and the three-dimensional complexity is lost. Microtomography has produced insightful information on the topology of cracks in the cement paste matrix and how they are deflected by the dispersed hard inclusions. We will report the on-going research on the imaging of cement paste exposed to freezing condition and of 3-dimensional cracks in mortar with alkali-aggregate reaction performed at the Hard X-ray Microtomography (XMT) located at beamline 8.3.2 at the ALS.

It is recognized that the deformation state, grain size, and development of foliation in granitic rocks used as aggregate in concrete influence the alkali-silica reaction. By performing an analysis of preferred orientation in conjunction with expansion tests, Monteiro et al[12] showed that there is a quantitative relationship between the degree of deformation and reactivity in granitic rocks. In this paper, we summarize our on-going microstructural characterization of reactive rocks by neutron diffraction and transmission electron microscopy (TEM), observing dislocations and determining dislocation densities of quartz grains in granitic rocks of different deformation states.

Soft X-ray Microscopy

Soft X-ray microscopy uses advances in nanotechnology providing the tools and methodology to fabricate X-ray optical components of highest quality. Fresnel zone plates i.e. circular gratings with a radially increasing line density, are used to focus the x-rays and therefore constitute the basis for performing X-ray microscopy since with a refractive index close to unity, conventional lenses cannot be applied. State-of-the-art Fresnel zone plate optics have now achieved a 15nm-spatial resolution[13, 14] . The optical design for the soft X-ray microscope used in this research is an X-ray analogue to a conventional light microscope, only using Fresnel zone plates for the condenser and objective lenses (see Figure 1). X-rays which are emitted from a bending magnet source propagate to a condenser zone plate which provides a partially incoherent hollow-cone illumination of the sample and acts, due to the wavelength dependence of its focal length, together with a pinhole close to the specimen as a monochromator with a spectral resolution $E/\Delta E \sim 500$. The current condenser zone plate has an outer diameter of about 9mm, about 50,000 rings, and an outermost zone width Δr of about 40nm.The X-rays penetrating the specimen are projected by a micro zone plate being positioned at its focal length downstream of the sample, onto an X-ray sensitive CCD to create a full-field image. The backside-illuminated, thinned CCD has 2048x2048 pixels with a physical pixel size of 13.5μm. Due to the high flux of synchrotron radiation typical exposure times per image are only a few seconds covering a field of view of

about 10 μm diameter at a magnification of about 2,500. The micro zone plate, i.e. the high resolution objective lens has a diameter of about 30-60μm, typically about 500 rings and an outermost zone width Δr down to 15nm which largely determines the spatial resolution that can be obtained in soft X-ray microscopy.

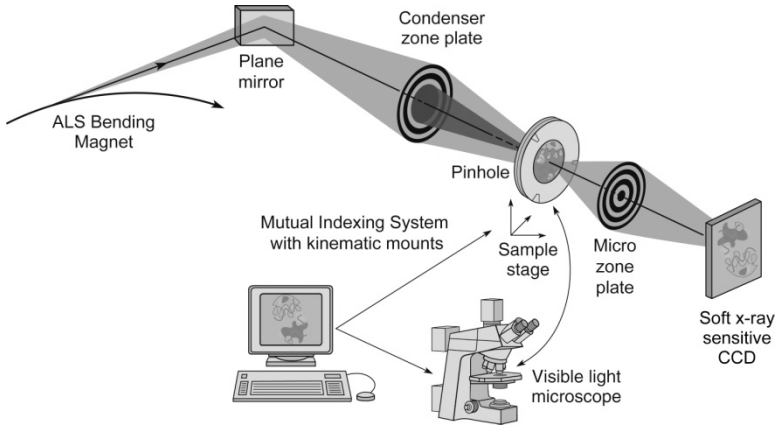

Figure 1 - Schematic layout of the soft X-ray microscopy beamline XM-1 at the ALS using X-rays emitted from a bending magnet. The micro zone plate projects a full field image onto a CCD camera that is sensitive to soft X-rays.

a) preparation of the solutions

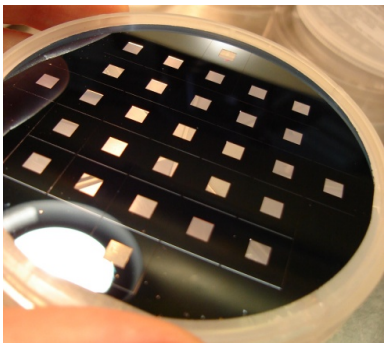

b) silicon nitride windows

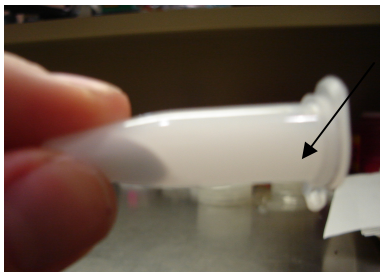

c) aspect of the supernatant solution after centrifugation

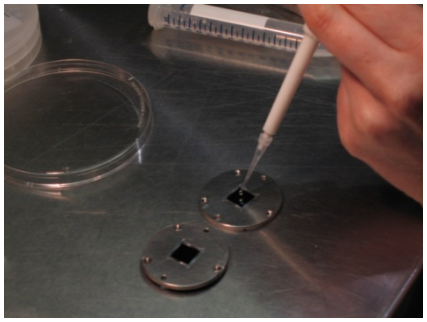

c) placement of the cement mixture into the windows

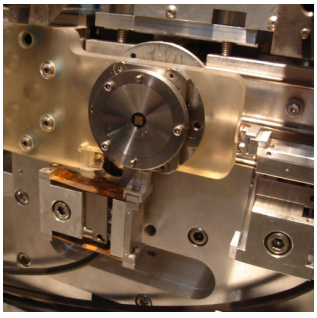

e) sample holder in the soft x-ray microscope

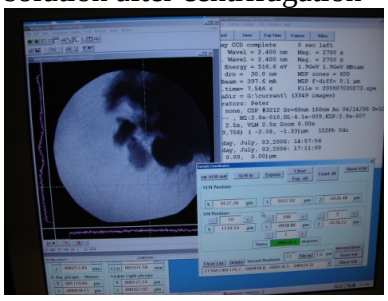

f) data acquisition

Figure 2 - Sequence of sample preparation

Figure 2 shows the main steps for the preparation of the samples used in soft x-ray microscopy. The samples must be highly diluted for the transmission of the soft X-rays. In order to retard the dissolution of the cement minerals in the highly diluted samples, and to provide calcium and sulfate ions for the reactions, a solution saturated with $Ca(OH)_2$ and $CaSO_4.2H_2O$ was used as the liquid media (pH=12.3). The solution was prepared using freshly boiled, deionized water inside a glove bag filled with nitrogen gas to avoid carbonation. Teflon and polyethylene flasks were used to prepare the solution to avoid alkali–silica reaction. The solid particles were mixed in the solution for 60 s inside a test tube and approximately 2 ml of the mixture was centrifuged for 15 s. A small droplet —around 2 µl—was taken from the supernatant with a micropipette and squeezed between two silicon nitride windows in a metallic sample holder that was then placed in the microscope for examination.

Images and results

Shrinkage of concrete on drying frequently leads to cracking. This is recognized in concrete design and construction practice, especially in regard to pavements, floors, and relatively thin structural members. To counteract this problem and reduce the restraint against shrinkage movements, shrinkage-compensating concrete containing expansive cements (e.g., Type K cement, which contains $C_4A_3\overline{S}$ as the principal source of the reactive aluminate) or expansive admixtures has been employed successfully for the last 30 years[15]. Expansive cements and admixtures unlike portland cement, expand during the early hydration period after setting. The expansion is a consequence of the formation of ettringite (calcium sulfoaluminate hydrate) in considerable quantities during the first few days of curing. Two different on-going tests are being conducted using soft x-ray microscopy and preliminary results are presented here.

In the first series of tests, the hydration of the $C_4A_3\overline{S}$ in a $Ca(OH)_2$ + $CaSO_4.2H_2O$ saturated solution was analyzed. The solution/solid materials ratio was 50 g/ml[3]. The morphology of this compound in absence and in presence of 10% of $Ca(OH)_2$ is presented over the time. Figures 3a and b show a sequence of large ribbons arranged in a fan-like or cross shape for a saturated $Ca(OH)_2$ solution, while in the presence of 10% $Ca(OH)_2$ the same ribbons are formed, but at a smaller size, which seems to be an apparently retardation of the $C_4A_3\overline{S}$ hydration.

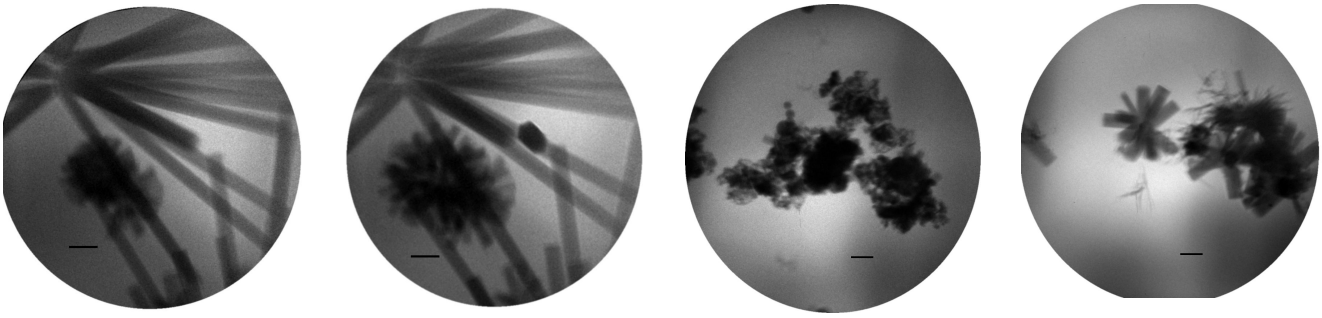

(a) 22min (b) 2h 45min (c)19 min (d) 2 h 47 min

Figure 3 - In situ soft x-ray images of hydrating $C_4A_3\overline{S}$ particles in a saturated calcium hydroxide-calcium sulfate solution, s/c= 50 cm^3/g ((a) and (b)) in presence of 10% $Ca(OH)_2$ ((c) and (e)). Hydration time is indicated. Scale bar corresponds to 1 µm

In the second series of tests, two types of expansive admixtures produced in Japan (calcium sulfoaluminate based cement) were blended with Type I-II cement. The purpose of the study was to analyze how these expansive materials work alone and in combination with Portland cement. Figure 4 shows soft X-ray images of Type I-II cement (Figure 4a) and pure expansive agents (Fig. 4b and c) after 35 minutes in solution. Figures 4d to g indicate how the type of expansive admixture modifies the microstructure. The solution/solid materials ratio was 10 cm^3/g.

As a result of combination between calcium, sulfate, aluminate, and hydroxyl ions within a few minutes of cement hydration, needle-shaped crystals of a calcium sulfoaluminate hydrate (ettringite) make their appearance as it can be seen in figure 4a; the shape of the particles formed by the two expansive admixtures are almost the same as seen on figure 4a. When cement is blended with 6% of expansive admixture, type 1 expansive admixture seems to form different compounds close to the surface of cement particles. It is important to notice that as the cement particles are formed by silicates and aluminates with addition of calcium sulfate, we can not exactly define which compound are present in these images.

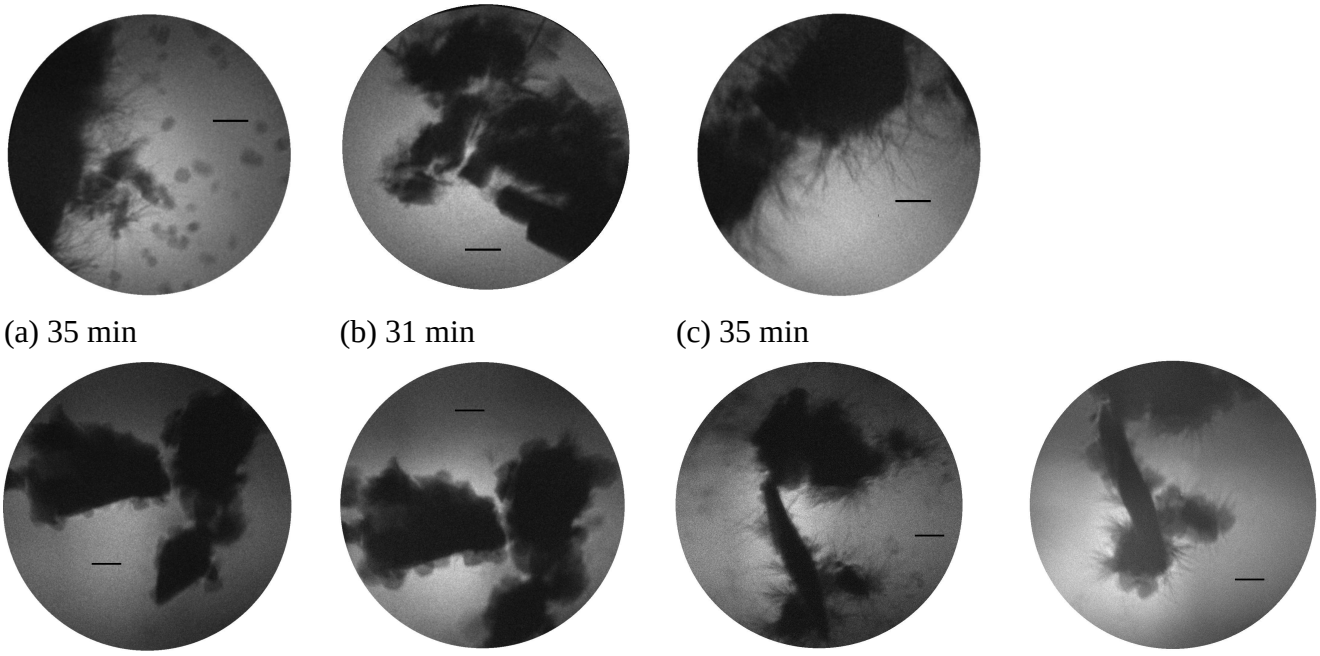

(a) 35 min (b) 31 min (c) 35 min

(d) 34 min (e) 55 min (f) 21 min (g) 1h 1 min

Figure 4 - a) In situ soft x-ray images of around 35 minutes hydration of type I-II cement, b) commercial expansive admixture type 1 hydrated for 31 minutes, c) commercial expansive admixture type 2 hydrated for 35 minutes, d and e) blend of type I-II cement and 6% of type 1 admixture at different hydration times f and g)) blend of type I-II cement and 6% type 2 admixture over the time in a saturated calcium hydroxide-calcium sulfate solution. Hydration time is indicated. Scale bar corresponds to 1 µm

X-ray Microtomography

In synchrotron XMT, a wide parallel X-ray beam passes through the sample and the transmitted fraction is detected as an image by a charge couple device (CCD) area detector. The sample is mounted on a stage with 4 degrees of freedom: x, y, and z transition for positioning and

centering of the sample, and rotation for data acquisition. The rotary stage allows for many X-ray transmission images of the sample to be recorded for a series of orientations. According to the Nyquist theorem, the minimum number of radiographs needed for a full reconstruction within 180 degrees of rotation is $N\pi/2$, where N is width of the sample in pixels. In practice little difference is observed for image numbers > $N\pi/4$.

At the ALS superbend beamline 8.3.2, the transmitted beam is detected by a scintillator that converts X-rays to visible light, which is imaged by magnifying lenses onto a CCD. The available optics allow for spatial resolutions between 0.44 μm/pixel and 11.5 μm/pixel. The monochromator is tunable to X-ray energies between 5 keV and 35 keV by means of a double multilayer mirror arrangement. The monochromator optics can also be removed from the beam allowing a white light mode of operation that is broadly polychromatic in the 30-70 keV range by means of metal filters.

Tomography imaging can be done either in absorption or phase contrast mode. In absorption mode, each pixel of the projection image represents the intensity of the transmitted beam that has not been absorbed by the sample. According to Beer's law :

$$I(x) = I_o\, e^{-\mu x} \tag{1}$$

Where I(x) is the final intensity of the beam after the beam passes through sample thickness x, I_o is the initial intensity of the beam, and μ is the material's linear attenuation coefficient, which can be expressed as:

$$\mu = \sum f_i \mu_i \rho \tag{2}$$

Where i represents each atomic element, f_i is the atomic weight fraction of the element in the material, μ_i is the mass attenuation coefficient at the beam energy, and ρ is the density of the material.

The attenuated value for each pixel, $P(\varphi, x')$. is then determined by:

$$P(\varphi, x') = -\ln\left[I(\varphi, x') / I_o(\varphi, x')\right] \tag{3}$$

Where for each angle of rotation for the sample, φ, x' indicates the axis parallel to the X-ray direction and perpendicular to the sample rotation. Furthermore, $I_o(\varphi, x')$ is the initial intensity of the beam, and $I(\varphi, x')$ is the intensity of the transmitted beam.

The attenuation can be expressed as an integral of the linear attenuation coefficient over the sample:

$$P(\varphi, x', z) = \iint_{\infty} \mu(x, y, z)\delta(x\cos\varphi + y\sin\varphi - x')dxdy \tag{4}$$

where the δ function defines the path of the X-rays through the sample, and μ is the material's linear attenuation coefficient. The function $P(\varphi,x',z)$ is known as the Radon transform or sinogram. Reconstruction involves inverting this equation to yield $\mu(x, y, z)$ at each voxel location[16]. Ultimately, the reconstruction procedure combines the 2D projection images to yield

a 3D data set of the absorbance of the sample at each voxel. The processed data contains a series of cross sectional slices (tomograms) at set height z of the sample.

The absorption mode scanning is usually applied with monochromatic light. If polychromatic beam is used, Beer's law no longer applies because the high-energy X-rays penetrate farther than those of low energy. This causes the beam hardening effect which makes the resulting image less quantitative. Mathematical approximations are required to work around the beam hardening effect. Only if one assumes that all components of the sample have the same energy dependence of absorption can one make a rigorous reconstruction.

The phase contrast mode relies on the variation of the real part of the index of refraction to provide image contrast. Materials differing in their refractive index affect differing phase shifts to the transmitted X-rays. The effect of the differing phase shifts is only seen at the edges between materials of different indices. The interaction of X-rays with differing phase shifts result in intensity cancellation or enhancement at the detector plane. Edges are seen as oscillating dark and bright lines and generally have much higher contrast than the corresponding absorption images. At X-ray wavelengths the index of refraction is about 10-100 times larger than the absorption index. Thus the phase contrast mode of operation can in principle be more sensitive than the absorption mode. Phase contrast tomography is harder to interpret quantitatively but progress is being made in this new area[17]. The phase contrast mode is useful for imaging light materials for which the absorption contrast is very small, such as for low density materials or for materials with very similar absorption properties but where small changes in refraction index can be observed.

With the radiograph size limit of 4000 pixels by 1000 pixels, and the source beam width being less than 4 cm, the choice of magnification becomes a tradeoff between the desired magnification and the scale of the sample to be tested. The sample must fit completely within the width of the produced radiograph, or else tomographic reconstruction becomes more approximate. A smaller sample can allow for greater magnification, and finer dimensions of the smallest observable detail. Smaller samples, however, deviate further from the reality of the material usage, as applications of concrete are generally for building large structures. Using larger samples, however, will come at a cost of lower magnification and coarser dimensions of the smallest observable particle size.

As an example of the application of microtomography to study the durability of concrete we will describe the current research of imaging the in-situ ice formation in entrained air-voids in hydrated cement paste. For this experiment, we performed XMT scans on air-entrained, hydrated cement paste cast in 0.25mm outer diameter glass capillary tube while subjecting the sample to several cycles of evaporated liquid nitrogen gas cooling and ambient thawing. To freeze the sample, we used an Oxford 600-series Cryostream. This unit, which is designed to cool small crystals for protein crystallography by the production of a jet of cold nitrogen gas with a coaxial outer sheath of dry nitrogen for frost prevention The scan settings were optimized for both absorption and phase contrast imaging. The absorption contrast provided imaging of the dense hydrated cement matrix, while the phase contrast provided imaging of the ice-air phases that would coexist in the partially filled air void. A 13 KeV monochromatic x-ray energy provided sufficient penetration through the hydrated cement paste, while an approximately 30 cm sample-to-detector distance enhanced the phase contrast imaging and made visible the ice-air interface within the air voids. The magnification was set at 5.4x with the resulting pixel size of 1.54 µm/pixel. Figure 5 shows a section through one of the cement air voids. The donut shape is the cement material constrained within the glass tube. Figure 5a is the frozen condition showing

indications of dendrtitic ice growth within the void, The sample was allowed to warm up to room temperature (Figure 5b) and the ice formation disappears, and then reappears with a different structure in Figure 5c on cool down. Figure 6 shows a 3-D reconstruction of the air/ice interface in a single air void – it is roughly that of a spherical shell. Upon thawing, the interface vanished, which confirmed the successful imaging of ice.

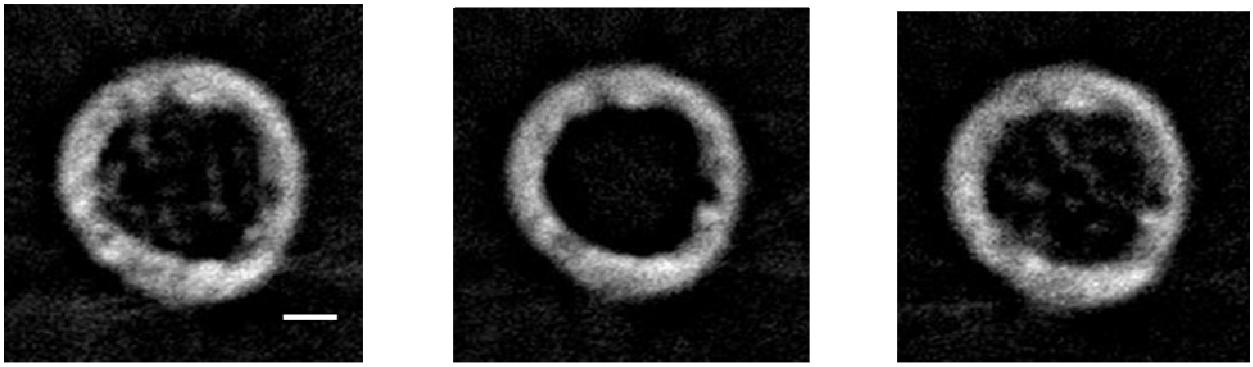

(a) First freeze (b) First thaw (c) Second Freeze

Figure 5 - Reconstructed tomograms of the sample in the midsection of one of the larger air voids. The scale bar is 50 µm. The ice crystals, believed to grow in dendritic form (a), disappear upon thawing (b) and reappear in changed morphology during the second freeze (c).

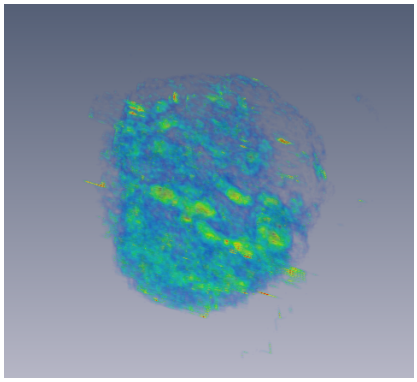

Figure 6 - A 3-D reconstruction of ice formation in a single air void. The cement matrix and the glass capillary have been removed via post reconstruction image processing. The air void is approximately 150 µm in diameter.

Microtomography is also useful at performing time scale experiments. As a second example of XMT application, we present a modified ASTM C1260 testing of aggregate reactivity. In this experiment, three 1”x1”x12” mortar bars were cast following the specifications of ASTM C1260, using known inert aggregate, while 50% of the aggregates by weight were substituted with partially strained quartz sand. The goal was to supplement the 2-week long gross numerical test method with visual representation of damage in progress. Considering the scale and the density of the sample, the samples were scanned under white beam filtered with aluminum plates and under low magnification. The resulting spatial resolution was 11.55µm/pixel. Furthermore, the scans were obtained under phase contrast mode in an attempt to enhance crack widths

smaller than spatial resolution. Since the 1”x1” cross section of the mortar bars was wider than the beam width, a narrower sample (0.75”x0.75”x9”) was cast. The large bars and the smaller bar were subject to the same conditions of testing as prescribed by the ASTM. The larger bars would provide the strain data while the smaller bar would be used for imaging. The smaller bar underwent slightly amplified, but comparable rate of expansion, and was therefore deemed to be a suitable representation of the standard-sized mortar bar expansion. Figure 7 shows internal sections of the same sample after 7 and 14 days. Close examination of the older sample shows the development of micro-cracks.

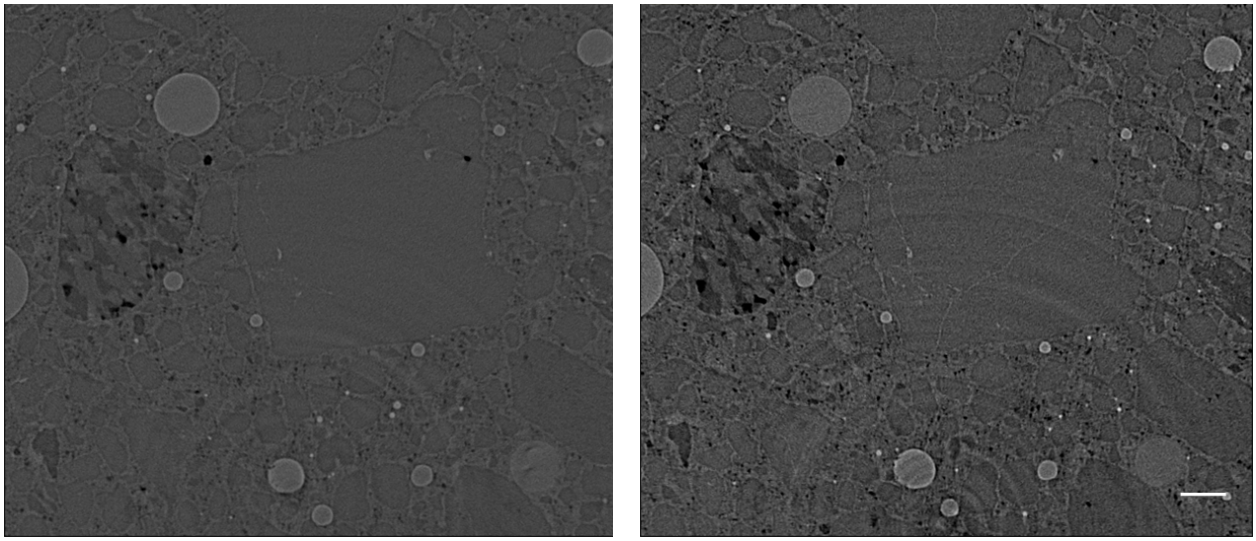

(a) 7 Days (b) 14 days

Figure 7 - Tomogram of reduced sized mortar bars at (a) 7 days and (b) 14 days of ASTM C1260 testing: New microcrack developments are visible. . The ring like structure overlayed on the images is an artifact of the tomographic reconstruction process. The scale bar is 500 µm.

Neutron Diffraction and Texture Analysis of Reactive Rocks

Alkali-silica reaction depends on more factors than simply the crystallinity of silica. It is relevant to stress the importance of texture analysis in the identification of reactive rocks. In many rocks, minerals exhibit a preferred orientation pattern, and this is expressed in anisotropy of physical properties. This “directionality”, also known as “texture” in materials science, develops, for example in metamorphic rocks, during ductile deformation. Rotations of crystals occur owing to intracrystalline slip by dislocation movements, and patterns may be modified during dynamic recrystallization. The orientation distribution of crystals is most commonly represented in pole figures. The pole figure is constructed by placing a polycrystalline sample inside a sphere and intersecting a crystal direction (e.g. the c-axis or [0001] of quartz) with the surface of the sphere producing “poles”. Pole densities can then be contoured and expressed as a smooth distribution, usually normalized such that contours express pole densities in multiples of a uniform distribution.

Crystal orientations can be measured with a petrographic microscope equipped with a universal stage or by x-ray diffraction with a pole figure goniometer. Both these techniques are

very limited for fine-grained polymineralic rocks. More advanced techniques are neutron and electron diffraction. Neutron diffraction has low absorption compared to x-rays and electrons. Therefore, large bulk samples, up to several centimeters in size can be measured and the measurements represent a good average of the bulk properties. Because of this, neutron diffraction has become the preferred technique to characterize texture properties of rocks and sophisticated methods have been developed to determine the crystal orientation distributions of the various components that constitute rocks. Since texture patterns are related to deformation state and the deformation state is related to expansion of concrete, the rock texture of the aggregate emerges as a useful parameter to predict concrete stability.

The rocks used for testing were obtained from the Santa Rosa mylonite zone in Southern California. This area is of great interest to mineralogists who quantified the processes that occurred during the transformation of granite to mylonite and phyllonite, particularly the development of preferred orientation, and the evolution of microstructure.

Figure 8 displays pole figures for quartz (a) and biotite (b) in order of increasing deformation. Biotite preferred orientation increases with increasing deformation from a maximum of 1.4 m.r.d. in weakly deformed granite (PC 715) to 12 m.r.d. in phyllonite (PC 92). (001) lattice planes become aligned in the schistosity plane with some bending around the lineation direction. Quartz preferred orientation also increases in strength as granite deforms to mylonite with a c-axis maximum in the intermediate fabric direction Y. This is a typical pattern in recrystallized quartzites and is regionally observed in Santa Rosa mylonites[18]. The maximum increases from 1.5 m.r.d. (PC 715) to 5.5 m.r.d. (PC 82). With further deformation and grain size reduction quartz textures attenuate and randomize in phyllonite.

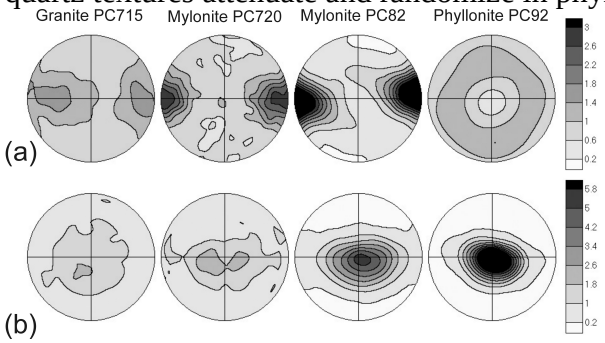

Figure 8 - Pole figures in order of increasing deformation. The pole figures for quartz 0001 (a) and biotite 001 (b) are projected onto the foliation plane, the macroscopic lineation is X, and the intermediate direction is Y. Linear scale (in m.r.d.), equal area projection.

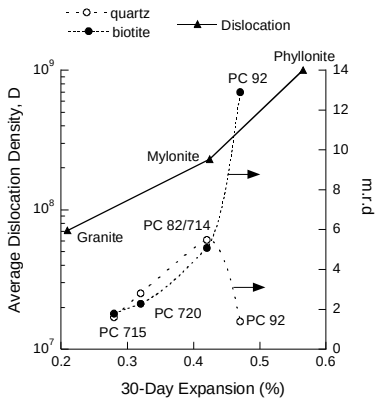

Figure 9 - Average dislocation density D and (001) pole figure maximum for quartz and biotite in multiples of a random distribution (m.r.d) as a function of the 30-day mortar expansion for each rock type.

Dislocation densities of each type of rock were measured by TEM. Figure 9 shows the log of the average dislocation density versus the average expansion percentage. This plot illustrates the positive correlation between mortar expansion dislocation density. This would suggest that dislocations have a strong effect on the reactivity of quartz bearing rocks with

respect to the ASR. Figure 9 also shows a plot of the quartz (0001) pole figure maxima versus the expansion % illustrating that no linear correlation exists between quartz texture and susceptibility to the alkali-silica reaction. Quartz texture increases during initial deformation. However, a change in the mechanism of stress accommodation at high deformation causes the preferred orientation of quartz to be destroyed[19, 20, 21, 22]. Unlike quartz, biotite texture increases with deformation. In Figure 9, a plot of the biotite (001) pole figure maximum versus expansion %, suggests a monotonic relationship between biotite texture and the susceptibility of quartz grains within the same rock to the alkali-silica reaction. Even though biotite is not a reactant in the alkali-silica reaction, it is commonly present in granitic rocks as an accessory mineral. Biotite texture may indicate quartz susceptibility to the alkali-silica reaction. Details of the experimental program can be found in Wenk et al[23].

Conclusions

Cement hydration behavior is complex principally in function of the dynamism and the conditioning of the reaction. This justifies the reason that diverse referring aspects to this subject are not yet total explained, principally because fast data acquisition is essential to adequately capture the complexities of the system. Thus, x-ray imaging by transmission soft x-ray microscopy affords some clear benefits for the characterization of cement-based materials as:

- Rapid data acquisition
- High (nanoscale) resolution
- Non-destructive examination
- Characterization of hydrated samples at normal temperature and pressure

Texture analysis of quartz grains showed no simple relationship between quartz preferred orientation and the susceptibility to the alkali-silica reaction. However, texture analysis of biotite, a common accessory mineral in granites, shows a linear relationship with reactivity. These results suggest that preferred orientation of biotite may be used to estimate the susceptibility of rocks containing both biotite and quartz to the alkali-silica reaction.

Acknowledgement

The soft X-ray microscope operation was supported by the DOE, Office of Science, Basic Energy Sciences, Division of Materials Sciences and Engineering. The Advanced Light Source is supported by the Director, Office of Science, Office of Basic Energy Sciences, of the U.S. Department of Energy under Contract No. DE-AC02-05CH11231. The authors would like to thank Cruz Carlos and Roula Rbeiz for their assistance in the ASTM 1260 preparation and testing. Paulo Monteiro acknowledges the financial support from the National Science Foundation grant 062464.

References

1. Kurtis, K. E., Monteiro, P.J.M., Brown, J.T., and Meyer-Ilse, W., 1998, Imaging of ASR gel by soft X-ray microscopy. Cement and Concrete Research 28 411-421.
2. Kurtis, K. Monteiro, P. J. M. MEYER-ILSE, W., 2000, Soft X-ray spectromicroscopy for in situ study of corrosion, Journal of Corrosion Science, s42 (8) 1327-1336.
3. Gartner, E. Kurtis, K. Monteiro, P. J. M., 2000, Proposed mechanism of C-S-H growth tested by X-ray microscopy, Cement and Concrete Research, 30 (5) 817-822.

4. Lamour V. H. R. Monteiro, P. J. M. Scrivener, K. L. Fryda, H., 2001, Microscopic studies of the early hydration of calcium aluminate cements. Proceedings of the Conference on Calcium Aluminate cements.
5. Kurtis, K., Collins, C.L. Monteiro, P. J. M., 2002, The surface chemistry of the alkali-silica reaction: A critical evaluation and X-ray microscopy, Concrete Science and Engineering, 4 1-11
6. Kurtis KE, Monteiro PJM, 2003, Chemical additives to control expansion of alkali-silica reaction gel: proposed mechanisms of control , Journal of Materials Science, 38 (9): 2027-2036.
7. Juenger, M.C.G. Lamour, V. Monteiro, P.J.M. Gartner, E.M. Denbeaux, G.P., 2003, "Direct observation of Cement hydration by X-ray microscopy", Journal of Materials Science Letters, 22(19) 1335-1337
8. Juenger, M.C.G. Monteiro, P. J. M. Gartner, E. M. Denbeaux, G. P., ., 2005 , A soft X-ray microscope investigation into the effects of calcium chloride on tricalcium silicate hydration, Cement and Concrete Research 35 (1) 19-25.
9. Silva, D.A. and Monteiro, P.J.M., 2005, Hydration evolution of C3S - EVA composites analyzed by soft X-ray microscopy, Cement and Concrete Research, 35(2) 351-357
10. Silva and Monteiro, 2006, Silva, D.A. and Monteiro, P.J.M. "The influence of polymers on the hydration of portland cement phases analyzed by soft X-ray transmission microscopy" Cement and Concrete Research, Volume 36, Issue 8, Pages 1501-1507
11. Silva, D.A. and Monteiro, P.J.M.., 2007, Early formation of ettringite in tricalcium aluminate – calcium hydroxide – gypsum dispersions, Journal of Ceramics Society, 90 [2] 614–617.
12. P.J.M. Monteiro, K. Shomglin, H.-R. Wenk, and N.P. Hasparyk, 2001, *ACI Materials Journal*, **98** 179.
13. W. Chao, B.H. Harteneck, J.A. Liddle, E.H. Anderson and D.T. Attwood, 2005, *Soft x-ray microscopy at a spatial resolution better than 15 nm*, Nature 435, 1210-1213
14. Kim, D.H., Fischer, P., Chao, W., Anderson, E., M.-Y. Im, S.-C. Shin, and S.-B. Choe, 2006, *Magnetic soft X-ray microscopy at 15nm resolution probing nanoscale local magnetic hysteresis (invited),* J. Appl. Phys. **99**, 08H303 (2006).
15. Mehta, P. K. Monteiro, P. J. **Microstructure, Properties and Materials**. McGraw-Hill, Third Edition, 2006. 659 p.
16. Kak. A.C., Slaney, M., 2001, "Principles of Computerized Tomographic Imaging", *Classics in Applied Mathematics*; **33**, Society for Industrial and Applied Mathematics, Philadelphia.
17. Groso, A., Abela, R., Stampanoni, M., 2006, "Implementation of a fast method for high resolution phase contrast tomography", *Optics Express*, **14**, 8103-8110.
18. Pehl J. and H.-R. Wenk, 2005, J. Struct. Geol. 27, 1741.
19. Goodwin L.B. and H.-R. Wenk, 1995, Journal of Structural Geology 17, 689.
20. Wenk H.R. and J. Pannetier, 1990, Journal of Structural Geology 12, 177.
21. Boullier A.M. and Y. Guegen, 1975, Contributions to Mineralogy and Petrology 23,128.
22. Behrmann J. H. and D. Mainprice, Techtonophysics 140 (1997) 297.
23. Wenk, H.-R. , P.J.M. Monteiro and K. Shomglin, 2008, *Journal of Materials Science*. 43:1278–1285.